Supporting Information:

Local Structure And Magnetism Of $La_{1-x}M_xPO_4$ (M=Sm, ^{239}Pu, ^{241}Am) Explained By Experimental And Computational Analyses

Laura Martel[1]*, Md. Ashraful Islam[2], Karin Popa[1], Jean-Francois Vigier[1], Eric Colineau[1], Hélène Bolvin[2], and Jean-Christophe Griveau[1]*

[1]European Commission, Joint Research Centre (JRC), 76125 Karlsruhe, Germany.

[2]Laboratoire de Chimie et Physique Quantiques, CNRS, Université Toulouse III, 118 route de Narbonne, 31062 Toulouse, France.

*lpm.martel@gmail.com

*jean-christophe.griveau@ec.europa.eu

Table of Contents

Notes

Figures

Tables

Note S 1: X-Ray Diffraction

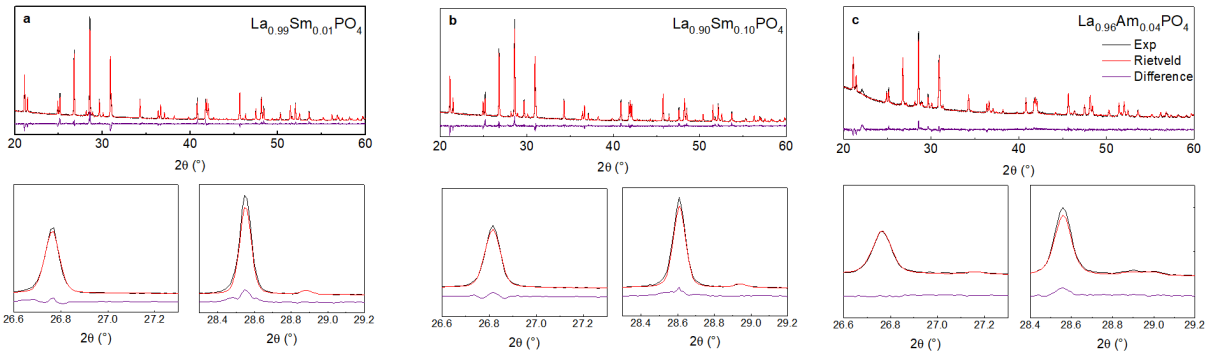

Figure S 1: XRD patterns of the $La_xSm_{1-x}PO_4$ and $La_xAm_{1-x}PO_4$ (day 0).

Note S 2: Relative intensities, experimental paramagnetic shifts and, definition pseudocontact (PCS) and Fermi contact shifts (FCS)

1. *Relative intensities Experimental and calculated considering a randomly distributed network (RDN)*

Table S 1: Experimental and calculated relative intensities (%) for $La_{1-x}Sm_xPO_4$.

	$La_{0.99}Sm_{0.01}PO_4$			$La_{0.962}Sm_{0.038}PO_4$			$La_{0.922}Sm_{0.078}PO_4$		
Peak Number	RDN	Exp	Err	RDN	Exp	Err	RDN	Exp	Err
1	93.2	93.04	1	76.5	76.5	1	60.1	60.8	1
2	5.6	5.63	1	15.9	16.3	1	22.9	23.1	1
3	0.9	1.33	0.2	6.3	6.1	1	9.1	9.7	1
4	--	--	--	1.36	1.2	0.2	7.2	6.4	0.2

Table S 2: Experimental and RDN relative intensities (%) for $La_{1-x}Pu_xPO_4$.

	$La_{0.988}Pu_{0.012}PO_4$			$La_{0.947}Pu_{0.053}PO_4$			$La_{0.88}Pu_{0.12}PO_4$		
Peak Number	RDN	Exp	Err	RDN	Exp	Err	RDN	Exp	Err
1	93.2	91.61	2	69.8	69.1	2	47.8	41.2	5
2	1.9	3	0.5	7.3	5.5	1	10.6	10.6	1
3	2.8	3.31	0.5	11	14.5	1	15.9	17.6	1
4	0.9	1.17	0.2	3.7	3.17	1	5.3	5	1
5	0.9	1.1	0.2	3.7	3.7	1	5.3	5.7	1

Table S 3: Experimental and RDN relative intensities (%) for $La_{0.96}Am_{0.04}PO_4$.

Peak Number	Exp	RDN	Err
1	72.8	73.5	4
2	6.8	6.61	1
3	8.9	9.91	2
4	4	3.3	1
6	0.7	--	0.1
5	3.3	3.3	1
7	1.3	--	0.5
8	2.1	--	0.5

2. Experimental paramagnetic shifts

Table S 4: ^{31}P NMR paramagnetic shifts for $La_{1-x}M_xPO_4$ (M= Sm, Pu, Am) obtained using the formula $\delta_p=\delta_{exp}-\delta_{dia}$ (with δ_{exp} from Table 1 and δ_{dia} is the value of peak 1).

Peak n°	$La_{1-x}Sm_xPO_4$			Peak n°	$La_{1-x}Pu_xPO_4$			Peak n°	$La_{1-x}Am_xPO_4$
	0.01	0.05	0.10		0.01	0.05	0.10		0.04
1	0	0	0	1	0	0	0	1	0
2	3.7	3.7	3.7	2	-23.4	-23.8	-24.3	2	27.3
3	6	6.2	6.2	3	-27.3	-27.2	-27.6	3	24.6
4		10	10	4	-44.2	-44.1	-44	4	54.9
				5	-65.3	-65.2	-65.3	5	83.1
				6		-52.3	-52.8	6	47.9
				7		-71.2	-71.6	7	111.4
				8		-92.4	-92	8	285.4
				9					

3. Temperature effect on the paramagnetic shifts

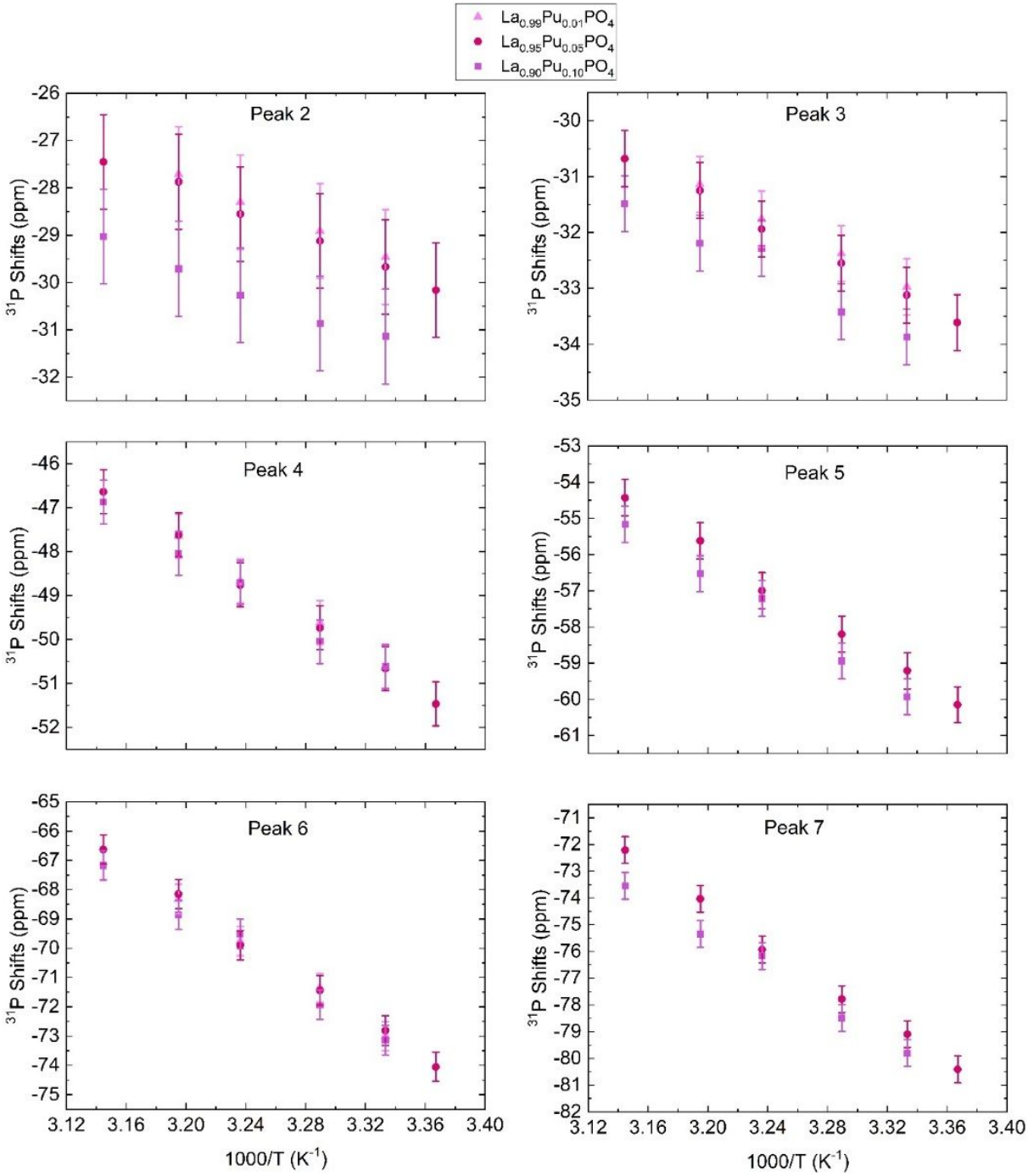

Figure S 2: Variation of the ^{31}P paramagnetic shifts with temperature T^{-1}.

The easiest way to detect the presence of a paramagnetic cation is by performing variable temperature experiments as it is an indication of a magnetic behaviour.[1] While the pseudocontact and Fermi contact interactions can be separated based on temperature in the rare-earth based compound, this statement does not stand for the actinide series[2,3]. Nonetheless, as it is a confirmation of magnetism often discussed in the literature, we present here our results. We varied the temperature between 295 K and 315 K (it is worth mentioning that we considered the temperatures based on an external thermometer and therefore a gradient might exist). For all compounds, the peak corresponding to the $P(OLa)_7$ species -Peak 1- is temperature

independent as there is no magnetic cation in the P vicinity. For the $La_xSm_{1-x}PO_4$, the paramagnetic shifts varied slightly (~0.5 ppm) for peaks 3 and 4 (not shown). For the $La_xPu_{1-x}PO_4$, the shifts varied up to 3 ppm (Figure S 2). Finally, for $La_{0.96}Am_{0.04}PO_4$, there was no shift variation in the range of temperature probed. Nonetheless, temperature dependency might exist over a wider range of temperature as only slight variations are expected (Previous authors reported ~11 ppm over a range of 150 K for $Am[(\{^{15}N\}C5\text{-}BPP)_3](OTf)_3$[4]).

4. Definition pseudocontact (PCS) and Fermi contact shifts (FCS)

The paramagnetic shift δ_p^K on the *K* nucleus has two contributions $\delta_p^K = \delta_{PCS}^K + \delta_{FCS}^K$,

i) The pseudocontact term δ_K^{PCS} associated with the through space dipolar interaction between the electronic magnetic moment of the nucleus and the nuclear magnetic moment of nucleus *K*. It is expressed in terms of the principal values χ_i of the magnetic susceptibility tensor[5]

$$\delta_{PCS}^K = \frac{1}{4\pi\, r_K{}^3} \frac{\left(3x_K{}^2 - r_K{}^2\right)\chi_x + \left(3y_K{}^2 - r_K{}^2\right)\chi_y + \left(3z_K{}^2 - r_K{}^2\right)\chi_z}{r_K{}^2}$$

#

Eq. S1

where x_K, y_K, z_K are the coordinates of nucleus *K* relative to the paramagnetic center and $r_K{}^2 = x_K{}^2 + y_K{}^2 + z_K{}^2$.

ii) The Fermi contact term δ_{FCS}^K related to the delocalization of the spin density of the paramagnetic cation towards the nucleus K through the bonds. The component $i, i = x,y,z$ is written as:[5,6]

$$\delta_{FCS,ii} = \frac{-\mu_B}{\hbar\gamma_K k_B T\, Q_0} \sum_I e^{\frac{-E_I}{k_B T}} \langle I \left| \hat{m}_i \right| I\rangle\langle I \left| A_{K,II}\hat{S}_{,i} \right| I\rangle + k_B T \sum_{J \neq I} \frac{\langle I \left| \hat{m}_i \right| J\rangle\langle J \left| A_{K,IJ}\hat{S}_{,i} \right| I\rangle}{E_J - E_I}$$

#

Eq. S2

where μ_B the Bohr magneton, k_B the Boltzmann constant, $\hbar$ the Planck constant, γ_K the nucleus magnetogyric ratio, $\hat{S}_i$ and $\hat{m}_i$ are the electronic spin and total magnetic moment operators, Q_0 the partition function, The sums run over the electronic states *I* with corresponding energy E_I and the $A_{K,IJ}$ represent the contact hyperfine coupling due to the presence of spin density at the nuclear position. In the case where this latter is supposed to be independent on the considered states, $A_{K,IJ} = A_K$, the hyperfine contact coupling constant, and Eq. S2 may be expressed as

$$\delta_{FCS,ii}^K = \frac{1}{\mu_0\gamma_K\mu_B} \frac{A_K}{\hbar}\, \chi_{iso}^S$$

Eq. S3

where χ_i^S is the spin contribution to the magnetic susceptibility. Finally, one gets

$$\delta_{FCS}^K = \frac{1}{3\mu_0\gamma_K\mu_B}\frac{A_K}{\hbar}\left(\chi_x^S + \chi_y^S + \chi_z^S\right)$$

Eq. S4

It can be expressed in terms in terms of the spin density at nucleus K $\rho^S(\boldsymbol{r_K})$ as

$$\delta_{FCS}^K = \frac{1}{3S}\chi_{iso}^S$$

Eq. S5

Note S 3:Experimental magnetic susceptibilities.

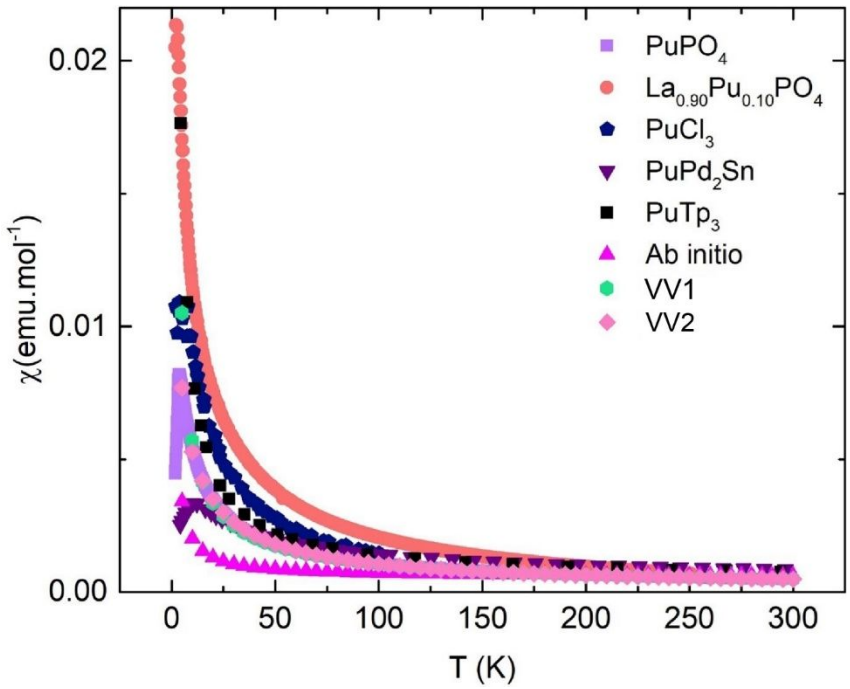

Figure S 3: Magnetic susceptibility curves of $La_{0.9}Pu_{0.1}PO_4$ and $PuPO_4$ recorded in the present study compared to the literature curves: $PuPd_2Sn$,[7] $PuCl_3$[8] and $PuTp_3$[9]. We also compared the theoretical curves determined by Ab initio calculations and fitting using the Van Vleck Eq. S6.

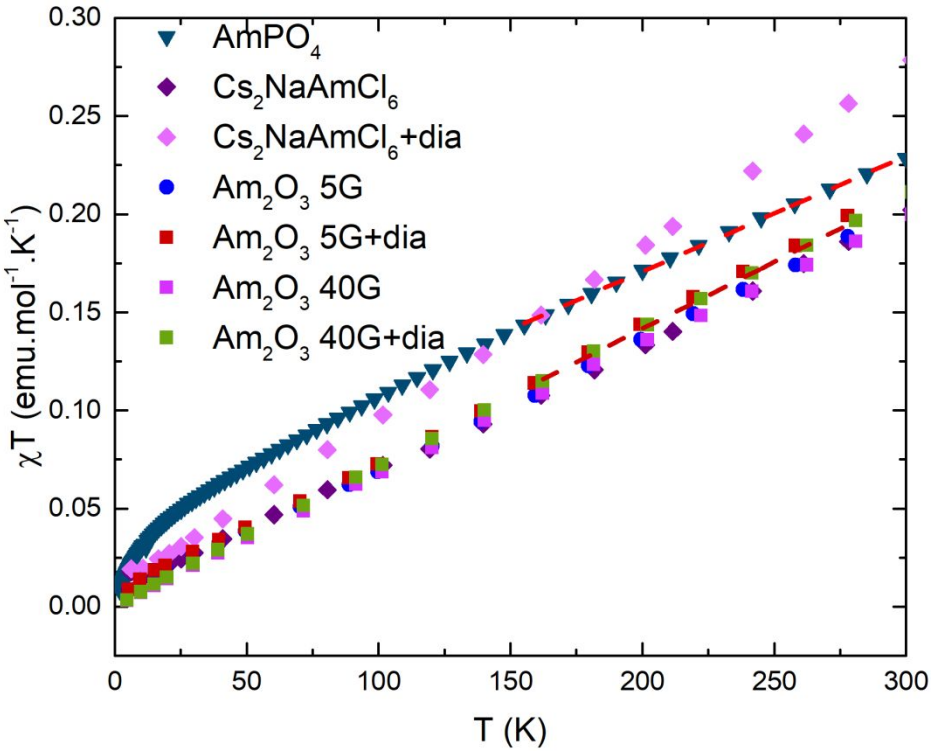

Figure S 4: Magnetic susceptibility of the Am-based materials. The data for $Cs_2NaAmCl_6$ and Am_2O_3 are extracted from reference 10. The linear fits corresponding to the temperature independent paramagnetism is of $5.8.10^{-4}$ emu.mol^{-1} for $AmPO_4$ and $6.9.10^{-4}$ emu.mol^{-1} for $Cs_2NaAmCl_6$ and Am_2O_3 corrected from the diamagnetic contribution.

Note S 4:Energy levels and Crystal Field Parameters.

In Table S 5, the energy of the levels calculated by the SF-CASSCF method. The ground term of the Sm^{3+} and Pu^{3+} free ions is a $^6H_{5/2}$. In the $[MLa_9(PO_4)_7]^{9+}$, the LS ^6H term splits by 500 and 1200 cm^{-1} at the SF-CASSCF level, for M=Sm and Pu, respectively. The ground term of the Am^{3+} free ion is a non-degenerate $^7F_0$ term. The LS ^7F term of the $[AmLa_9(PO_4)_7]^{9+}$ complex splits by 1200 cm^{-1}, as in the Pu^{3+} analogue. The larger splitting in the actinide complex denotes the larger interaction between the cation and the ligand in actinide complexes.[3,11]

Table S 5: SF-CASSCF energies (in cm^{-1}) of the $[MLa_9(PO_4)_7]^{9+}$ complexes (M^{III}).

M= Sm^{III}		Pu^{III}		Am^{III}		
sextets	quartets	sextets	quartets	septets	quintets	triplets
0	22342	0	16252	0	18608	33462
6	22345	71	16278	328	18689	33527
275	22441	621	16390	439	18713	33558
284	22448	695	16449	578	18781	33662
327	22486	842	16483	1087	18826	33674
363	22489	975	16497	1200	20536	33711
390	22500	1050	16537	1270	20557	33751
418	22513	1150	16619		20606	33773

450	22539	1169	16690	20643	33805
498	22554	1212	16720	20737	33912
512	22566	1238	16752	20785	
6928	22594	5289	16796	20855	
6943	22649	5418	16823	20925	
6971	22670	5509	16831	20940	
7029	22700	5562	16951	21038	
7048	22709	5589	16963	21072	
7088	22732	5690	17025	21121	
7124	22742	5810	17039	21130	
31305	22747	21947	17104	21224	
31646	22754	22669	17153	21245	
31684	22792	22741	17182		
	22796		17201		
	22807		17248		
	22823		17303		

In Table S 6, we report the energy of the levels calculated by the SO-CASSCF method. The $^6H_{5/2}$ term splits by 250 cm^{-1} in $[SmLa_9(PO_4)_7]^{9+}$, and the introduction of spin quartets in the state interaction does not influence on the results. On the contrary, for the Pu^{III} complex, the splitting of the ground term depends on the number of spin quartets included in the calculation, due to a large *J* mixing. For actinide complexes, the inclusion of dynamical correlation as for example CASPT2, is necessary to approach quantitative results.

Table S 6: SO-CASSCF energies (in cm^{-1}) of the $[MLa_9(PO_4)_7]^{9+}$ complexes (M^{III}). The number of SF states included in the state interaction is specified.

Sm^{III}		Pu^{III}				Am^{III}	
21sext	21sext-100quar	21sext	21sext-75quar	21sext-100quar	21sext-150quar	7sept-25quin	7sept-20quin-10trip
0	0	0	0	0	0	0	0
0	0	0	0	0	0	988	1627
186	179	383	453	271	363	1321	1965
186	179	383	453	271	363	1357	1988
254	239	504	649	439	500	3205	4378
254	239	504	649	439	500	3327	4489
910	1068	1760	2622	2500	2667	3383	4551
910	1068	1760	2622	2500	2667	3447	4631
988	1140	1922	2812	2645	2824	3646	4825
988	1140	1922	2812	2645	2824	5981	7333
1103	1263	2207	3143	3037	3116	6001	7344
1103	1263	2207	3143	3037	3116	6014	7401
1135	1296	2302	3270	3151	3225	6075	7466
1135	1296	2302	3270	3151	3225	6105	7509
2034	2324	3955	5590	5396	5602	6135	7531
2034	2324	3955	5590	5396	5602	6141	7598
2090	2376	4077	5716	5507	5721	8171	9854
2090	2376	4077	5716	5507	5721	8381	10075

2186	2470	4261	5944	5700	5914	8435	10189
2186	2470	4261	5944	5700	5914	8599	10258
2230	2520	4407	6051	5846	6016	8839	10322
2230	2520	4407	6051	5846	6016	8874	10407
2258	2549	4501	6191	5966	6133	8984	10437
2258	2549	4501	6191	5966	6133	9033	10506
3390	3717	6573	8407	7789	8188	9218	10726
3390	3717	6573	8407	7789	8188	10080	12640
3445	3773	6709	8523	7899	8298	10113	12644
3445	3773	6709	8523	7899	8298	10641	12909
3532	3858	6850	8718	8100	8439	10681	12947
3532	3858	6850	8718	8100	8439	10772	12995
3587	3913	6917	8786	8160	8547	10943	13072
3587	3913	6917	8786	8160	8547	11082	13112
3612	3938	7037	8882	8272	8630	11419	13189
3612	3938	7037	8882	8272	8630	11474	13221
3637	3962	7172	9061	8435	8723	11585	13273
3637	3962	7172	9061	8435	8723	11660	13308
4983	5207	7660	9724	8515	8789	11760	14869
4983	5207	7660	9724	8515	8789	11829	14875
5062	5287	8123	9972	8652	8916	12324	15286
5062	5287	8123	9972	8652	8916	12510	15313

In order to quantify the effect of the number of quartets and the dynamical correlation, the $[PuCl_6]^{3-}$ complex was used as a benchmark (see Table S 7). It shows that the splitting of the ground $^6H_{5/2}$ term is very sensitive to the quartets and to dynamical correlation and a large number of quartet states is necessary. While the SO-CASSCF reduced to the sextet states gives a splitting of 223 cm^{-1}, it is reduced to 39 cm^{-1} with quartets and doublets and dynamical correlation. It should be noted that the energy gap between the $^6H_{5/2}$ and $^6H_{7/2}$ manifolds is affected by the doublets. Since this level of description is not possible for a cluster as large as $[PuLa_9(PO_4)_7]^{9+}$, the energies were fitted on the experimental curves, but the nature of the states, as characterized by the g factors are taken from the SO-CASSCF calculation.

Table S 7: Energies (in cm^{-1}) of the $[PuCl_6]^{3-}$ complex, from CAS based calculations and experiment. Numbers in parentheses denote the degeneracy of the state.

		SF-CASSCF	SF-CASPT2		SO-CASSCF			SO-CASPT2			SO-CASSCF [11]	SO-NEVPT2 [11]	Exp [12]
	dege			dege	21Sext	21Sext-31Quar	21Sext-96Quar-31Doub	21Sext	21Sext-31Quar	21Sext-80Quar-31Doub	all	all	
sextets	3	0	0	2	0	0	0	0	0	0	0	0	0
	2	320	257	4	223	215	77	223	210	39	47	91	13-76
	3	435	406	2	1719	1757	2342	1696	1736	2446			

	3	968	1124	2	1895	1894	2634	1874	1860	2829
	3	5047	3216	4	1959	1989	2635	1988	2016	2809
	1	5228	3336	2	3892	3877	5139	3854	3829	5514
	3	5230	3724	4	4079	3919	5360	4085	3873	5805
	3	22012	15994	4	4132	4019	5463	4156	3992	5947
quartets	3	16034	13288	4	6626	5968	7496	6127	5062	7878
	1	16043	13526	2	6720	6048	7750	5470	5404	8372
	3	16115	13304							
	1	16229	13674							
	3	16270	13712							
	3	16307	14034							
	2	16495	14113							
	3	16582	14124							
	1	16606	14301							
	3	16709	14339							

Therefore, the energy gaps were determined by fitting the experimental χT curve, as described below. A Van Vleck (VV) equation for the three lowest Kramers Doublets (KD) arising from the *J*=*5/2* term writes[13]:

$$\chi T = \frac{N_A \mu_0 \mu_B^2}{3} \frac{1}{Q_0}\left[M_1^2 + M_2^2 e^{-\frac{\Delta_2}{k_B T}} + M_3^2 e^{-\frac{\Delta_3}{k_B T}} + \right.$$
$$\left. 2\, k_B T\left\{M_{12}^2 \frac{1 - e^{-\frac{\Delta_2}{k_B T}}}{\Delta_2} + M_{13}^2 \frac{1 - e^{-\frac{\Delta_3}{k_B T}}}{\Delta_3} + M_{23}^2 \frac{e^{-\frac{\Delta_2}{k_B T}} - e^{-\frac{\Delta_3}{k_B T}}}{\Delta_3 - \Delta_2}\right\}\right] + \chi_{TIP} T$$

Eq. S6

where N_A is Avogadro constant, μ_0 the vacuum permeability, μ_B the Bohr magneton, k_B the Boltzmann constant, Q_0 the partition function, Δ_2 and Δ_3 the energy gaps for KD2 and KD3 with the ground state, respectively. M_I^2 characterizes the magnetic moment of KDI, with $M_I^2 = \frac{1}{2}\left(g_{I,1}^2 + g_{I,2}^2 + g_{I,3}^2\right)$, $g_{I,i}, i = 1,2,3$ the three *g*-factors of KDI and M_{IJ}^2 characterizes the magnetic coupling between KDI and KDJ with $M_{IJ}^2 = \|\mathbf{M}_{x,IJ}\|^2 + \|\mathbf{M}_{y,IJ}\|^2 + \|\mathbf{M}_{z,IJ}\|^2$ and $\mathbf{M}_{i,IJ}, i = x,y,z$ the block magnetic moment matrix within the *I* and *J* manifolds, in terms of μ_B.

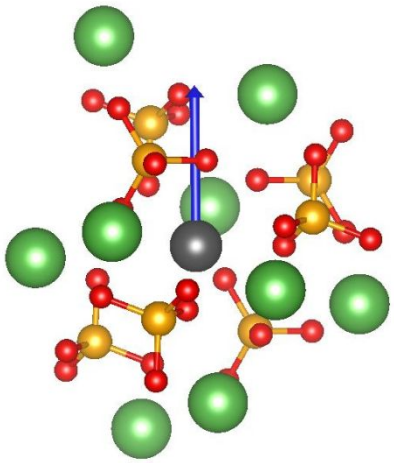

Figure S 5: Direction of the main principal axis of the ground Kramers Doublet (KD) of the $[PuLa_9(PO_4)_7]^{9+}$ complex, from SO-CASSCF (21sext-150quar).

The direction of the principal axis of the g tensor for the ground KD with the largest g value is presented in Figure S 5 and the g-factors values are reported in Table S 8.While the energy gaps vary with the numbers of SF states included in the state interaction, the composition of the three KDs is roughly unaffected (Table S 9). According to the SO-CASSCF results, expressed in the principal axes frame of the **g** tensor of KD1, KD1 is by 91% $M_J = \pm 5/2$, KD2 by 82% $M_J = \pm 3/2$ and KD3 by 78% $M_J = \pm 1/2$. In other terms, with a quantization axis taken as the magnetic axis of KD1, the three KDs can be approximated by pure M_J states. This is confirmed by Table S 9, where the magnetic factors appearing in Eq. S6 are similar. The fit of χT vs T was performed considering pure M_J: this permits the determination of three parameters, Δ_2, Δ_3 and χ_{TIP} . Only the points above 3 K were considered. We obtained two solutions with different orderings of the states. For the 1st solution, the $M_J = \pm 1/2$ doublet is the ground state, and the $M_J = \pm \frac{5}{2}$ and $M_J = \pm 3/2$ doublets lie 21 and 92 cm^{-1} above, respectively. For the 2nd solution, the $M_J = \pm 3/2$ doublet is the ground state, and the $M_J = \pm \frac{5}{2}$ and $M_J = \pm 1/2$ lie 15 and 83 cm^{-1} above, respectively. The two fits obtained are called VV1 and VV2 respectively in Figure S 3 and are remarkably similar. The fit with the magnetic moments issued from the *ab initio* calculations leads to roughly the same energies. It shows that there is a low-lying doublet at around 20 cm^{-1}, a much lower value than the SO-CASSCF one. It confirms that, as in the $[PuCl_6]^{3-}$ complex, the J mixing plays a key role to determine the low-lying states.

Table S 8: g-factors of the three first Kramers Doublets in the $[MLa_9(PO_4)_7]^{9+}$ complexes determined from SO-CASSCF calculations.

	Sm^{III}			Pu^{III}											
	21sext			21sext			21sext-75quar			21sext-100quar			21sext-150quar		
	g_1	g_2	g_3	g_1	g_2	g_3	g_1	g_2	g_3	g_1	g_2	g_3	g_1	g_2	g_3
KD1	0.99	0.16	0.06	0.62	0.12	0.22	1.05	0.17	0.01	1.16	0.12	0.21	1.13	0.20	0.03
KD2	0.66	0.40	0.10	0.52	0.18	0.82	0.66	0.29	0.41	0.74	0.14	0.39	0.73	0.48	0.22

KD3	1.19	0.67	0.04	1.28	0.45	0.19	1.28	0.64	0.00	1.11	0.81	0.09	1.28	0.65	0.04

Table S 9: Magnetic parameters (in μ_B^2) for the three lowest Kramers Doublet in the $[PuLa_9(PO_4)_7]^{9+}$ complex calculated with SO-CASSCF with 21sextets and 150quartets. They are compared to pure M_J KD1= $\pm$ 1/2; KD2= $\pm$ 3/2 KD3= $\pm$ 5/2.

	M_1^2	M_2^2	M_3^2	M_{12}^2	M_{13}^2	M_{23}^2
pure M_J	0.77	0.36	1.02	0.65	0	0.40
SO-CASSCF	0.71	0.35	0.95	0.56	0.12	0.62

Finally, the crystal field parameters (CFPs) were determined from CASSCF calculations according to the ITO procedure [14,15]. They depend on the Cartesian frame in which the molecule is described. The $[MLa_9(PO_4)_7]^{9+}$ complexes are rather spherical and there is no obvious choice for the z axis. According to the SO-CASSCF calculation, the **g** tensor of the ground KD is axial, but with small values of *g*. The crystal field strength parameter *S* defined as:

$$S = \sqrt{\frac{1}{3}\sum_{k=2,4,6}\frac{1}{2k+1}\sum_{q=-k}^{k}\left|B_q^k\right|^2}$$

Eq. S7

allows to evaluate the strength of ligand field with only one parameter. It is furthermore rotation invariant. In the following, we will restrict the discussion of the ligand field to this parameter, and to its derivatives of kth order. The CFPs originate from the position and nature of the ligands. Their original formulation concerns the orbital level, but they can be deduced from a LS or a J manifold. In the latter case, the CFPs are effective parameters that incorporate other physical effects, as electron-electron interaction and *J* mixing. For lanthanide complexes, the CFPs are similar for those different schemes[15,16] but might differ for actinide complexes, especially once the spin-orbit coupling is considered.

Table S 10: Strength parameters (total and of 2nd, 4th and 6th orders, in cm^{-1}) in the $[MLa_9(PO_4)_7]^{9+}$ complexes. They are deduced using the ITO procedure from the ground *L* manifold at SF-CASSCF level, from the ground *J* manifold at SO-CASSCF level, or from the fit of the experimental curve according to Eq. S6.

	Sm^{3+}		Pu^{3+}				Am^{3+}
	SF-CASSCF	SO-CASSCF	SF-CASSCF	SO-CASSCF	fit1	fit2	SF-CASSCF
S	234	286	585	535	208	127	545
S^2	279	284	523	438	2	54	527
S^4	206	407	541	816	360	360	479
S^6	209		677	223			619

The strength parameters are summarized in Table S 10. The comparison between the SF-CASSCF and SO-CASSCF parameters allows to gauge the effect of J mixing. S is worth 230 cm^{-1} for the Sm^{3+} complex and is more than twice larger for its actinide counterpart, due to larger covalent effects. It is slightly smaller for the Am^{3+} complex, following the usual trend within a series. The strength parameters of different orders S^k follow the same trends. With spin-orbit coupling, CFPs can not be calculated from the ground state of the Am^{3+} complex since it has a non-degenerate ground state with J = 0. From the J = 5/2 manifold, they can be calculated up to the 4^{th} order. While S is about the same from SO-CASSCF as from SF-CASSCF, the strength parameter deduced from the fitted values for Pu^{3+} is lower since the splitting of the states is largely reduced. And finally, the strength parameter of the actinide complex is smaller than its lanthanide counterpart.

Note S 5:Magnetic Susceptibility tensors, pseudocontact shifts and Mulliken charges

1.1. Magnetic susceptibility tensors

The magnetic susceptibility tensors deduced from SO-CASSCF results as summarized in Table 2. In order to evaluate the interaction with the excited J manifolds, different SO spaces were considered: all states, the ground and first J manifolds (J;J+1), and only the ground J manifold (GS J), except for the Am^{III} complex where J=0 leads to a non-magnetic state. For the three complexes, the J;J+1 space provides results similar to all space, but different from the GS J space. It shows that the states higher that the J+1 manifold do not contribute quantitatively to the magnetic susceptibility, while the J+1 manifold contributes qualitatively. This latter manifold is not statistically populated and contributes by 2nd order Zeeman interaction with the GS J manifold. The orbit and spin contributions, χ^L and χ^S, are evaluated by replacing the total magnetic moment by its orbit or spin counterpart contribution.

1.2. The calculated pseudocontact shifts

Table S11: Pseudocontact contribution to the paramagnetic shifts δ_{PCS} (in ppm) at 309 K in the complexes $[AnLa_9(PO_4)_7]^{9+}$ using Eq. S1. The P atoms are labelled according to Figure 6.

P site	Sm^{III}	Pu^{III}	Am^{III}
P1	2.82	1.24	-2.61
P2	6.65	2.99	11.79
P3	3.01	1.05	-1.77
P4	-1.99	-0.97	-1.80
P5	-5.87	-2.44	-3.10
P6	6.04	2.73	10.87
P7	-5.85	-2.50	-3.91

2. Mulliken charges.

Table S12: Mulliken charges (*1000) on the P atoms, total ($q(P)$) and in the s-orbitals ($q_s(P)$), from CASSCF calculations in the complexes $[MLa_9(PO_4)_7]^{9+}$ (M^{III}). The P atoms are labelled according to Figure 6.

P site	Sm^{III}		Pu^{III}		Am^{III}	
	$q(P)$	$q_s(P)$	$q(P)$	$q_s(P)$	$q(P)$	$q_s(P)$
P1	0.09	0.00	0.34	0.01	0.40	0.10
P2	0.23	0.03	0.89	0.09	0.97	0.18
P3	0.12	0.02	0.70	0.11	0.85	0.16
P4	0.12	0.02	0.54	0.10	0.55	0.12
P5	0.14	0.01	0.70	0.09	0.85	0.10
P6	0.18	0.02	0.81	0.10	0.88	0.14
P7	0.14	0.03	0.63	0.16	0.65	0.12

Supporting References

1 Palke, A. C.; Stebbins, J. F., Paramagnetic interactions in the ^{31}P NMR spectroscopy of rare earth element orthophosphate ($REPO_4$, monazite/xenotime) solid solutions, *Am. Miner.*, **96**, 1343–1353 (2011).

2 Autillo, M.; Guerin, L.; Bolvin, H.; Moisy, P.; Berthon, C. Magnetic susceptibility of actinide(III) cations: an experimental and theoretical study, *Phys. Chem. Chem. Phys.*, **2016**, *18*, 6515-6525.

3 Autillo, M., *et al.*, Insight of the metal–ligand interaction in f-element complexes by paramagnetic NMR spectroscopy, *Chem. Eur. J.*, **2019**, *25*, 1-18.

4 Adam, C., Beele, B. B., Geist, A., Müllich, U., Kaden P. & Panak, P. J., NMR and TRLFS studies of Ln(III) and An(III) C5-BPP complexes, *Chem. Sci.*, **2015**, *6*, 1548-1561.

5 Bertini, I., Luchinat, C., Parigi, G., Magnetic susceptibility in paramagnetic NMR, *Prog. Nucl. Magn. Res. Sp.*, **2002**, *40*, 249-273.

6 Kurland, R. J. & McGarvey, B. R., Isotropic NMR shifts in transition metal complexes: The calculation of the fermi contact and pseudocontact terms, *J. Magn. Reson.*, **2**, 286(1970).

7 Gofryk, K.; Kaczorowski, D.; Griveau, J-C.; Magnani, N.; Jardin, R.; Colineau, E.; Rebizant, J.; Wastin, F.; Caciuffo, R. Extensive studies of antiferromagnetic $PuPd_2Sn$, *Phys. Rev. B*, **2008**, *77*, 014431.

8 Jones Jr., E. R.; Hendricks, M. E.; Stone, J. A.; Karraker, D. G., Magnetic properties of the trichlorides, tribromides, and triiodides of U(III), Np(III), and Pu(III), *J. Chem. Phys.*, **1974**, *60*, 2088.

9 Magnani, N., Colineau, E., Griveau, J.-C., Apostolidis, C., Walter, O., Caciuffo, R., A plutonium-based single-molecule magnet, *Chem. Commun.*, **2014**, *50*, 8171-8173.

10 Soderholm L.; Edelstein N.; Morss L.R.; Shalimoff, G. V. The magnetic behavior of trivalent americium compounds, *J. Magn. Magn. Mater.*, **1986**, *54-57*, 597-598.

11 Jung, J.; Atanasov, M.; Neese, F., Ab initio ligand-field theory analysis and covalency trends in actinide and lanthanide free ions and octahedral complexes, *Inorg. Chem.*, **2017**, *56*, 8802-8816.

12 Carnall, W.T., A systematic analysis of the spectra of trivalent actinide chlorides in D3h site symmetry, *J. Chem. Phys.*, **1992**, *96*, 8713.

13 Autillo, M.; Islam, M. A.; Héron, J.; Guérin, L.; Acher, E.; Tamain, C.; Illy, M.-C.; Moisy, P.; Colineau, E.; Griveau, J.-C.; Berthon, C.; Bolvin H. Temperature dependence of ^1H paramagnetic chemical shifts in actinide complexes, beyond Bleaney's theory. The $An^{VI}O_2^{2+}$ dipicolinic acid complexes (An=Np, Pu) as an example, *Chem. Eur. J.*, **2021**, *27*, 7138-7153.

14 Ungur, L.; Chibotaru, L. F. Ab Initio crystal field for lanthanides, *Chem. Eur. J.*, **2017**, *23*, 3708–3718.

15 Jung, J.; Islam, M. A.; Pecoraro, V. L.; Mallah T.; Berthon, C.; Bolvin, H., Derivation of Lanthanide Series Crystal Field Parameters From First Principles, *Chem. Eur. J.*, **2019**, *25*, 15112-15122.

16 Alessandri, R.; Zulfikri, H.; Autschbach, J.; Bolvin, H., Crystal field in rare-earth complexes: from electrostatics to bonding, *Chem. Eur. J.*, **2018**, *24*, 5538-5550.